1 **Correlations between variations in Solar EUV and soft X-ray**
2 **irradiance and photoelectron energy spectra observed on Mars**
3 **and Earth**

4

5 W.K. Peterson[1], D.A. Brain[1], D.L. Mitchell[2], S.M. Bailey[3], and P.C.
6 Chamberlin[4]

7 [1]LASP, University of Colorado, Boulder

8 [2]SSL, University of California, Berkeley

9 [3]Baradley School of Engineering, Virginia Tech.

10 [4]Solar Physics Laboratory, NASA Goddard Space Flight Center, Greenbelt, Md.

11

14

15

Abstract:

17

18 Solar extreme ultra violet (EUV; 10-120 nm) and soft X-ray (XUV; 0-10 nm) radiation

19 are major heat sources for the Mars thermosphere as well as the primary source of

20 ionization that creates the ionosphere. In investigations of Mars thermospheric chemistry

21 and dynamics, solar irradiance models are used to account for variations in this radiation.

22 Because of limited proxies, irradiance models do a poor job of tracking the significant

23 variations in irradiance intensity in the EUV and XUV ranges over solar rotation time

24 scales when the Mars-Sun-Earth angle is large. Recent results from Earth observations

25 show that variations in photoelectron energy spectra are useful monitors of EUV and

26 XUV irradiance variability. Here we investigate photoelectron energy spectra observed

27 by the Mars Global Surveyor (MGS) Electron Reflectometer (ER) and the Fast Auroral

28 SnapshoT (FAST) satellite during the interval in 2005 when Earth, Mars, and the Sun

29 were aligned. The Earth photoelectron data in selected bands correlate well with

30 calculations based on 1 nm resolutions observations above 27 nm supplemented by broad

31 band observations and a solar model in the 0-27 nm range. At Mars, we find that

32 instrumental and orbital limitations to the identifications of photoelectron energy spectra

33 in MGS/ER data preclude their use as a monitor of Solar EUV and XUV variability.

34 However, observations with higher temporal and energy resolution obtained at lower

35 altitudes on Mars might allow the separation of the solar wind and ionospheric

36 components of electron energy spectra so that they could be used as reliable monitors of

37 variations in solar EUV and XUV irradiance than the time shifted, Earth based, $F_{10.7}$

38 index currently used.

39 **Introduction:**

40

41 The primary energy source driving the inner planetary ionospheres and

42 thermospheres of Venus, Earth, and Mars is solar extreme ultra violet (EUV; 10-121 nm)

43 and soft X-ray (XUV; 0-10 nm) radiation. Solar irradiance varies with solar longitude on

44 solar cycle, solar rotation, and solar flare time scales. Uncertainties in EUV and XUV

45 irradiance illuminating Venus, Earth, and Mars limit the usefulness of thermospheric

46 codes in studies of their atmospheres (e.g. Gronoff et al., 2012). To be useful in

47 thermospheric and ionospheric codes, solar irradiance observations and/or models should

48 have high spectral and temporal resolution (See for example, Richards et al., 2006,

49 Peterson et al., 2008, Qian et al., 2010, and Lollo et al., 2012) and either use proxies

50 taken within a narrow range of solar longitudes facing the planet of interest or provide a

51 correction due to solar center to limb variations (Qian et al, 2010). Almost all solar

52 irradiance observations are made at the Earth and have both observational biases and

53 spectral and temporal limitations (e.g. Chamberlin et al., 2007, 2008, Peterson et al.,

54 2012). Most solar irradiance data is available on the web site:

55 http://lasp.colorado.edu/lisird/. When used at Mars solar proxies driving these models are

56 shifted in time to account for the different range of solar longitudes illuminating Mars

57 (e.g. Fox and Yeager, 2006).

58   Peterson et al., [2009, 2012] have demonstrated that daily averaged photoelectron

59 energy spectra obtained from the Fast Auroral SnapshoT (FAST) satellite (Carlson et al.,

60 2001) at Earth have observable spectral variations in response to variations in solar EUV

61 and XUV variations. They have compared observed and modeled daily averaged

62 photoelectron energy spectra and have shown that the disagreement between observed

63 and modeled photoelectron energy power in five selected energy bands is on the order of

64 30% over solar rotation time scales. This was done using models of solar irradiance

65 variations in the 0-50 nm range derived from spectrally limited and temporally sparse

66 Thermosphere, Ionosphere, Mesosphere, Energetics, and Dynamics (TIMED) / Solar

67 Extreme Ultraviolet Experiment (SEE, Woods et al., 2005) observations.

68   Because Earth based observations are available and directly relevant, the

69 uncertainties in incident EUV and XUV irradiance at Mars are comparable to those at

70 Earth during periods of alignment when the Mars-Sun-Earth angle is small (i.e. less than

71 ~30°). At other times there are few, if any, solar irradiance observations at Mars.

72 Significant additional uncertainty in the solar irradiance at Mars is introduced because the

73 standard Earth derived proxies for solar irradiance models have to be time shifted to

74 account for the rotation of a solar features seen on Earth to be seen on Mars. See, for

75 example, Mitchell et al., 2001, Jain and Bhardwaj [2011] and Gronoff et al., [2012].

76 During periods of non-alignment the uncertainties in EUV and XUV irradiance energy

77 input to Mars are so large that it is reasonable to consider the possibility of using

78 variations in photoelectron intensity on Mars to monitor variations in incident solar EUV

79 and XUV fluxes. The purpose of this paper is to investigate this possibility. This paper

80 presents comparisons of variations in electron energy spectra observations from the Mars

81 Global Surveyor (MGS) Electron Reflectometer (ER, Acuña et al., 1992, 2001, Mitchell

82 et al., 2001, Brain et al., 2007) with those observed in the photoelectron electron energy

83 spectra at Earth detected by FAST. Suitable MGS/ER data are available from 1997 to

84 2006; suitable FAST data are available from 1997 to 2009. The comparisons are made

85 during the interval in 2005 when Earth, Mars, and the Sun were aligned.

86   The paper is organized as follows. We first describe the relative positions of active

87 regions on the Sun with respect to Earth and Mars late 2005. We then briefly review the

88 technique developed by Peterson and his colleagues to relate variations in solar irradiance

89 with variations in photoelectron energy in selected energy bands and apply this to data

90 obtained from the FAST satellite at Earth during the interval of interest. This is followed

91 by a discussion of how this technique has to be modified to accommodate differences in

92 the plasma environment around Mars and features of electron observations made in this

93 environment by the MGS/ER. We discuss the limitations of the MGS/ER Martian

94 observations and conclude with a discussion on what electron observations might be used

95   to monitor variations in solar EUV and XUV energy input to the Martian thermosphere

96   and ionosphere.

Observations:

97

98

99   *Sun*

100   In the fall of 2005 the Sun, Mars, and Earth were nearly aligned and there was

101   recurring solar activity monitored by the Extreme Ultraviolet Imaging Telescope (EIT)

102   on NASA's Solar and Heliophysics Observatory (SOHO). Figure 1 shows SOHO EIT

103   Carrington maps from synoptic full-disk data from the iron line at 17.1 nm for Carrington

104   rotations 2034 (9/4 to10/1 2005) and 2035 (10/1 to 10/28 2005). Time runs from right to

105   left in Carrington rotation synoptic maps. See, for example, Ulrick and Boyden (2006) for

106   information on how these synoptic maps are created. SOHO data were not available

107   before 9/15. Two features in the solar data are indicated. The first was seen nearest the

108   center of the solar disk on September 24 and again on October 20. The second was seen

109   nearest the center of the solar disk on October 12.

110

111   Figure 2 presents more information about the spectral, spatial, and temporal

112   evolution of the irradiance seen at Earth and Mars for the period from September 1 to

113   October 16, 2005. The green line in Panel A indicates the Earth-Sun -Mars angle as a

114   function of time. Panel A also shows the angles of the two solar features identified in

115   Figure 1 as seen from Earth and Mars. Feature 1 is shown in solid lines; feature 2 is

116   shown with dotted lines. Red lines indicate Mars; black lines indicate Earth. Panels B, C,

117   and D present the $F_{10.7}$, MgII, and GOES X-ray proxies of solar activity as measured on

118   the Earth (See, for example, Chamberlin et al., 2008). The dotted vertical lines appear for

119   September 13 and 24 and October 12, the days features identified in Figure 1 are closest

120   to the center of the Sun's disk observed from Earth. Panel A shows that variations in

121   solar irradiance during this interval associated with activity at the features seen near the

122   center of the Sun's disk was seen simultaneously at both Earth and Mars. A detailed look

123   at the observations from which the Carrington displays shown in Figure 1 were

124   constructed shows that solar activity was not limited to the two regions identified and that

125   some of the activity was near the solar limbs, which would not be visible simultaneously

126   on Earth and Mars.

127   Panels B, C, and D in Figure 2 illustrate the diverse variations in solar irradiance

128   proxies obtained at Earth used to drive various solar irradiance models. Until the launch

129   of NASA's Solar Dynamics Observatory (SDO) spacecraft in 2010 (Woods et al., 2010)

130   variations in solar irradiance were sparsely sampled as a function of time and wavelength.

131   Chamberlin and his colleagues have used proxies of solar irradiance variations and solar

132   irradiance observations to construct a model of solar irradiance at high temporal (60s)

133   and spectral (1 nm) resolution. This Flare Irradiance Spectral Model (FISM, Chamberlin

134   et al., 2007, 2008) has been shown to agree well with observed variations in

135   photoelectron intensity seen at solar flare, solar rotation, and solar cycle time scales

136   [Peterson et al., 2008, 2009, 2012]. In the next sub-section we compare and contrast

137   photoelectron observations with those calculated using the FISM model for the interval

138   shown in Figures 1 and 2.

139

140   *Earth*

141   Peterson et al., [2008, 2009, and 2012] have shown how to assemble and compare

142   observed and modeled photoelectron energy distributions and relate them to variations in

143   solar irradiance over various time scales. The observations are all from an electron

144   spectrometer on the FAST spacecraft [Carlson et al., 2001]. The data used were obtained

145   at latitudes below the auroral zone and at altitudes above 1500 km. Data processing

146   included correction for the spacecraft potential, removal of the background signal, and

147   creation of daily averages to improve the signal to noise ratio at the highest energies. For

148   comparison with observations, Peterson et al., [2012] used two photoelectron production

149   codes driven by five different solar irradiance models to investigate uncertainties in solar

150   energy input to the thermosphere on solar rotation time scales.

151   Figure 3 presents and compares observed and modeled photoelectron spectra at Earth

152   for the interval shown in Figures 1 and 2 using the techniques and some of the models

153   described in Peterson et al., [2012]. Panel A shows the daily average observed escaping

154   flux of photoelectrons as a function of energy from 10 eV to 1 keV encoded using the

155   color bar on the right. Vertical black lines are drawn the same dates highlighted in

156   Figures 1 and 2. Since most of the variation in photoelectron flux intensity is seen above

157   about 30 eV, it is convenient to display photoelectron energy spectra as a function of

158   equivalent wavelength. Equivalent wavelength is calculated from the Planck relation

159   between energy and frequency assuming a constant 15 eV ionization potential as

160   described by Peterson et al., [2008]. Panel B shows the observed daily averaged

161   photoelectron power density in the same 5 equivalent wavelength bands used by Peterson

162   et al., [2008, 2009, and 2012] as a function of time. The power density in units of W/m^2

163   is encoded by the color bar on the right. Panel C shows the relative difference between

164   the observations shown in panel B and the average as a function of equivalent wavelength

165   observed over the entire interval. The relative difference is encoded using the color bar

166   on the right. Here relative difference = (observations – average) / average. If the

167   observations were constant, the relative difference would be 0 and Panel C would be

168   solid green. During two intervals, before about September 16 and centered on October 14,

169   relatively more intense photoelectrons were observed below ~10 nm (above about 100

170   eV) than on average. We note, and discuss further below, that the variations seen in the

171   GOES X-ray fluxes in Panel D of Figure 2 follow a similar pattern of intensity variation

172   with time.

173   Panel D of Figure 3 presents calculated daily average photoelectron power density in

174   the same 5 equivalent wavelength bands. The daily average is calculated from model

175   calculations made at the times and locations of the observations. Here we use the FISM

176   model solar irradiance spectrum and the Field Line Interhemispheric Plasma model (FLIP,

177   Richards, 2001, 2002, 2004, and references therein). Panel E show the relative difference

178   between the observations and the photoelectron spectrum calculated using the

179   FLIP/FISM model pair. Here relative difference = (observations – calculations) /

180   observations. The difference is encoded using the color bar on the right. If the

181   observations and calculations agreed at all times and equivalent wavelengths Panel E

182   would be solid green. On average the agreement between the observed and calculated

183   fluxes is quite good especially above ~20 nm equivalent wavelength where solar

184   rotational variability is less (Peterson et al., 2012). We note, and discuss further below,

185   that not all of the variations are completely captured by the FLIP/FISM model pair nor do

186   they follow variations in the solar $F_{10.7}$ index shown in Panel F.

187

188   *Mars*

189   The limitations to FAST observations of photoelectron spectra at Earth are detector

190   sensitivity and noise introduced by high-energy particles. The MGS/ER reflectometer is

191   more sensitive than the FAST electron spectrometer (Acuña et al., 1992; Carlson et al.,

192   2001). The noise introduced in electron measurements by high-energy particles is

193   significantly less at Mars. At Earth there are large regions where photoelectrons are well

194   isolated from solar wind, auroral, and cusp electrons. The Mars magnetic field is not as

195   strong and well organized as it is at Earth. In some regions of the sunlit hemisphere, the

196   crustal magnetic field is strong enough that the MGS spacecraft (at ~400 km altitude)

197   travels through closed field lines anchored in the crust, and ionospheric photoelectrons

198   dominate. In other regions, the crustal field is weak, and the spacecraft travels through

199   draped solar wind magnetic field lines, where both solar wind and ionospheric electrons

200   can be present, depending on the minimum altitude sampled by the field line. The

201   complex and time variable distribution of crustal magnetic cusps represent a third

202   possibility.   Consequently, the separation of solar wind and ionospheric photoelectrons at

203   Mars is not as complete and depends on time and location. At Mars the presence of one

204   or more features in the electron spectra are used to identify photoelectron spectra. These

205   features are associated with HeII 30.4 nm emissions (Frahm et al, 2007), Auger electrons

206   (Mitchell et al., 2000) and the sharp decrease in solar irradiance below ~16 nm (e.g.

207   Peterson et al., 2012). The identification of photoelectrons on Mars is now routinely used

208   to identify boundaries between the Martian ionosphere and the shocked solar wind. See,

209   for example, Mitchell et al., [2000 and 2001], Liemohn et al., [2003], Frahm et al., [2006

210   and 2007], Brain et al., [2007] and Dubinin et al., [2006 and 2008].

211   To provide a reliable monitor of variations in solar EUV and XUV irradiance,

212   Martian electron spectra used must have a minimal solar wind electron component. Here

213   we use details of the observed energy and angular distributions to attempt to identify

214   electron distributions with minimal solar wind electron content. It is well known that for

215   an energy dependent range of angles around 90° pitch angle the signal to any electron

216   detector is contaminated by blockage by and/or photoemissions from spacecraft surfaces

217   (e.g. Peterson et al., 2009). Liemohn et al., (2003) have developed a pitch-angle

218   dependent photoelectron production and transport code. Their analysis shows that the

219   best model data comparisons are possible for field-aligned electrons. For these reason

220   pitch angle resolved data from the MGS/ER are considered here. The electron

221   reflectometer has 30 logarithmically spaced energy steps from 10 eV to 20 keV. The 8

222   steps from 10 to 100 eV are all resolved in pitch angle. Pitch angle data from the

223   remaining 22 steps are averaged over two adjacent energy steps, for a total of 19 pitch

224   angle resolved energy bands. In the mapping orbit data considered here the radii of

225   curvature of electrons for these 19 energy steps in the magnetic fields encountered are

226   large compared to spacecraft dimensions. We exclude from the analysis data acquired in

227   the 7 of the 16 angular sectors looking toward the spacecraft. To improve the signal to

228   noise ratio at the highest energies we consider daily average Martian photoelectron fluxes.

229   Figure 4 presents the pitch angle resolved electron energy spectra obtained on

230   September 20, 2005 as a function time. Panels A-E display pitch angle ranges $0-30^{\circ}$, 30-

231   60°, 60-120°, 120 -150°, and 150 -180° respectively over the energy range from 11 eV to

232   1 keV. The flux intensity is encoded using the color bar on the right. A three-step process

233   is used to obtain photoelectron spectra from MGS/ER data obtained from September 14

234   through December 15, 2005. The first step is to filter data based on location where they

235   were acquired. We select spectra obtained only when the solar zenith angle at the satellite

236   was less than 90°. To focus on photoelectrons produced deeper in the ionosphere and

237   close to the sunlit satellite we require that the magnetic declination (i.e. angle of the

238   magnetic field from the local horizontal) was greater than 30° or less than -30°. For the

239   data acquired on September 20, 2005 in the 0-30° pitch angle range 1080 spectra were

240   selected for further processing. For the 30-60° range it was 1718; for the 60-120° range it

241   was 1979; for the 120-150° range it was 1531; and for the 150-180° range it was 934. We

242   corrected for the spacecraft potential using comparisons of observed energy spectra with

243   those calculated using a modified GLOW code (Solomon and Qian, 2005 and references

244   therein) that included CO_2 cross sections provided by Dr. Jane Fox and a neutral

245   atmosphere provided by Dr. Ian Stewart. As expected we found that the correction for the

246   spacecraft potential was less than a few volts.

247   Next, for each day of data, we examined the ratios of electron fluxes at selected

248   pairs of energy steps to identify electron data that have characteristic photoelectron

249   flux energy distributions. Our filter uses the 19 energy steps for which pitch angle

250   information is available. It is adapted from filter used by Brain et al., [2007] to

251   identify photoelectron energy spectra using 30 energy step omnidirectional data.

252   Figure 5 shows the 1080 electron energy spectra obtained in the 0-30° pitch angle

253   range on September 20, 2005. One hundred six of these spectra, shown in orange,

254   passed the shape filter based on ratios of fluxes at the energies indicated by the

255   dotted vertical lines. The daily average of the 106 selected spectra in the 0-30° range

256   is indicated by the green line. Data for the 4 other pitch angle ranges are also

257   processed in this way.

258   Examination of several days of data that pass the daily energy step filter showed

259   that a small number of spectra with relatively high fluxes in the 20 eV range were

260   passing the 19 energy step photoelectron shape filter described above. These energy

261   spectra represent a mixture of shocked solar wind and ionospheric photoelectrons.

262   We therefore applied a third filter on the MGS/ER data to improve separation of

263   photoelectron spectra and those mixed with shocked solar wind plasma. Figure 6

264   presents the 7353 electron spectra obtained from September 14 to December 15

265   that passed the daily shape filter for pitch angles between 0° and 30°. The third filter

266   uses the distribution of flux intensity at 20 eV in 20 bins. It rejects spectra that are in

267   intensity bins that contain at least 5% of the spectra with the highest flux at 20 eV.

268   The fraction rejected depends on the shape of the intensity distribution. The flux

269   level corresponding to the intensity bin selected is indicated by the horizontal blue

270   line in Figure 6. The 6603 spectra that have the flux intensity at 20 eV below the cut

271   off level are selected for further processing. The green spectra shown in Figure 6 is

272   the average of the 6603 spectra passing the third filter. The same third filter is

273   applied to data in the other 4 pitch angle ranges.

274   To see what, if any, pitch angle variation there is in the photoelectron energy

275   spectra selected using the process described above, we examined the scatter of flux

276   values at selected energies. Figure 7 shows scatter plots of the flux intensity at 30 eV

277   as a function of altitude. The solid horizontal lines show the average flux. The pitch

278   angle ranges are color coded as indicated. Data for the 0–30° range was plotted last

279   and over plots data from other pitch angle ranges. Visual inspection shows that the

280   scatter of the data in the 0-30° range is lower. The observations reported here are

281   made in the altitude range from ~370 to ~430 km, well above the region of peak

282   photoelectron production. At this altitude there are two possible geometries for

283   observing photoelectrons: 1) on field lines with both feet in the ionosphere below

284   (i.e. the trapped geometry), 2) on field lines with only one foot in the ionosphere (i.e.

285   the open geometry). In the trapped geometry photoelectrons are observed at both

286   0° and 180° pitch angles, i.e. from both the "near" and "far" feet of the field line. In

287   this geometry the flux of photoelectrons reflected back from the opposite feet of the field

288   lines is small and decreasing above ~20 eV (Richards and Peterson, 2008). Since the

289   focus of this paper is on variations in solar illumination, contributions to the flux from

290   reflections are not relevant because the reflected component does not vary strongly with

291   energy.

292   We note that auroral acceleration has been observed associated with the closed

293   magnetic field geometry (Bertaux, et al., 2005). These processes modify the

294   photoelectron spectra significantly; they are rejected by our filters. There are many

295   possible reasons for the large scatter of data points seen in Figure 7. The most

296   probable one is that the procedure outlined above to select photoelectron spectra is

297   not perfect. Another reason for relatively more scatter at pitch angles between 30°

298   and 150° is that the relatively large cross section for electron scattering on CO_2 are

299 magnified by variations in effective path length at larger pitch angles. For these

300 reasons the rest of this paper focuses on the Martian 0-30° pitch angle data.

301   Figure 8 presents the filtered MGS/ER data from September 14 to October.

302 Panel A shows all photoelectron energy spectra in the 0-30° pitch angle range. The

303 continuity in time of the data Panel A is an artifact of the display software. A varying

304 number of photoelectron spectra were obtained per day as shown in Panel D. Panel

305 B shows the daily average photoelectron intensity in the same 5 energy bins used in

306 Figure 3 as a function of equivalent wavelength. Panel C shows the relative difference

307 between the observations shown in panel B and the average as a function of equivalent

308 wavelength observed over the entire interval. The relative difference = (observations –

309 average) / average. If the observations were constant, the relative difference would be 0

310 and Panel C would be solid green.

311   Figure 8 shows some, but not all, of the same temporal and spectral variations

312 of photoelectron intensity seen in Panel C of Figure 3. The data for October 5 appear

313 to be significantly more intense than those obtained on the adjacent days.

314 Examination shows that 9 photoelectron spectrum in the 0-30° pitch angle range

315 passed our filter process while over 150 were available on the adjacent days.

316 **Comparison of photoelectron spectra from Earth and Mars**

317

318   Figures 3 and 8 illustrate the similarities and differences between variations

319 seen at Earth and Mars in photoelectron intensity during an interval when the

320 Earth-Mars-Sun angle is small and there is modest solar activity. Figure 9 presents

321 the 106 Mars MGS/ER filtered photoelectron energy spectra (orange) and the 96

322 Earth FAST photoelectron energy spectra (black) acquired on September 20, 2005.

323 The daily average FAST spectrum is indicated in red and that for Mars in green. The

324 red + symbols in Figure 9 show the 1 standard deviation uncertainty in the average

325 Earth flux value based on the number of counts detected. At energies above ~500 eV

326 the daily average Earth photoelectron fluxes are below the instrumental detection

327 threshold. The solid red line at the bottom is the instrument background of the Mars

328 electron detector. The observed Martian photoelectron fluxes are well above

329 background over the energy range displayed.

330   There is a remarkable difference in the scatter in the two data sets in Figure 9 at

331 energies above about 100 eV. This difference arises because the MGS/ER has two

332 selectable entrance apertures, which cover the same field of view but differ in their

333 transmission by a factor of 43.5 [Acuña et al., 1992, Mitchell et al., 2001]. The FAST

334 electron spectrometer has a constant geometric factor, which results in relatively

335 fewer counts at the highest energies. For this reason Peterson et al., [2009, 2012]

336 use daily average spectra to improve the signal to noise ratio above 25 eV where the

337 variations in solar EUV and XUV intensity below 30 nm produce the most variability

338 in photoelectron energy spectra.

339   The shape of Mars photoelectron energy spectra reported here depends on

340 details of production and transport processes and on imperfections in the

341 photoelectron filtering process described above, which can lead to some solar wind

342 electron contamination in the selected spectra. The shape of Earth photoelectron

343   energy spectra depends on the correction for background and counting statistics.

344   The relative magnitudes of photoelectron fluxes observed on Earth and Mars also

345   depends on solar irradiance. Solar irradiance scales as $1/R^2$, where R is the distance

346   from the Sun. On September 20 the irradiance at Earth was 1.97 times more intense

347   than at Mars. The ratio of photoelectron intensities as a function of energy shown in

348   Figure 9 is, however, not uniform with energy. The ratio is about 3 at 300 eV and

349   increases non-uniformly to about 7 at 20 eV. Some of this variation can be attributed

350   to instrumental uncertainties in the FAST data above about 100 eV. However

351   differences in production and transport processes associated with dominant

352   Nitrogen-Oxygen atmosphere at Earth and dominant CO_2 atmosphere at Mars must

353   also be considered. Doering et al., [1976] and Lee et al., [1980a, b] have documented

354   the variation in the shape of Earth's photoelectron energy spectrum as a function of

355   altitude for solar minimum conditions. Spectral peaks in the energy distribution

356   from photoionization of the dominant species by intense HeII at 30.4 nm can be

357   resolved in the production region below about 200 km but are significantly

358   broadened by scattering process when they are observed at higher altitudes at

359   Earth and Mars (Doering et al., 1976, Frahm et al., 2007). The Doering and Lee

360   papers also show relatively small (compared to the differences between Mars and

361   Earth spectra seen in Figure 9) changes in the slope of the photoelectron energy

362   spectrum between 20 and the 100 eV upper limit of the sensitivity of the

363   Atmosphere Explorer photoelectron spectrometers.

364   The focus of this paper is not on the energy dependence of photoelectron

365   spectra in different atmospheres. Rather it is on the relationships between

366   variations in photoelectron energy fluxes in limited energy ranges to variations in

367   solar EUV and XUV irradiance as indicated in spectrogram format in panel C of Figures

368   3 and 8. Figure 10 presents the relative difference between the observed and

369   average Earth (black) and Mars (orange) photoelectron power in the 5 equivalent

370   wavelength bands used by Peterson et al., (2009, 2012). The green lines shown in

371   Figure 10 are from the calculations based on the photoelectron energy spectra calculated

372   using the FLIP model with solar irradiance input from the FISM model presented above

373   in panel E of Figure 3. Visual inspection of Figure 10 shows intervals of several days

374   where the relative differences of photoelectron intensity at Earth and Mars have

375   similar variations over a few days. For example the relative differences in the

376   highest energy (3 nm, Panel A) Earth and Mars band from September 19 to 29 are

377   similar. Also the relative differences in Earth observations closely follow

378   calculations based on the FLIP/FISM model pair (green lines) in Panels C, D, and E.

379   The correlation between the variations in photoelectron intensity in selected bands

380   measured at Earth and Mars shown in Figure 10 can be quantified by calculating

381   correlation coefficients. Data from both Earth and Mars are available for 31 of the 45

382   days shown in Figure 10. Table 1 presents the correlations coefficients between

383   observations at Earth and various quantities including observations at Mars. Also shown

384   in Table 1 are the correlations between variations in the intensity of photoelectrons at

385   Earth in selected energy bands and the $F_{10.7}$, GOES X-ray, and MgII indices proxies for

386   solar EUV and XUV irradiance variability. Because continuous Earth based data are

387   available, these correlations are for the full 45-day interval between September 1 and

388   October 15.

389   The correlations between photoelectron observations at Earth and Mars shown in the

390   third column of Table 1 are weak to moderate. That is the correlation coefficients are in

391   the range from 0.2 to 0.6. They vary from a maximum of 0.57 in the 7 nm band to 0.20 in

392   the 13 nm band. The correlations between photoelectron observations at Earth and those

393   calculated using the FLIP/FISM model pair are, however, moderate to very strong,

394   varying from a low of 0.4 in the 7 nm band to a high of 0.93 in the 13 nm band. The last

395   three columns of Table 1 show weak to moderate (0.01 to 0.69) correlations between

396   observations at Earth and three of the most common Earth based proxies for solar EUV

397   and XUV variation.

398   The weak to moderate correlation between photoelectron observations at Earth and

399   the $F_{10.7}$, MgII index, and the daily maximum power in the 0.7 nm X ray flux measured

400   on NOAA's GOES satellites is well known and documented. See, for example,

401   Chamberlin et al., (2007, 2008). The FISM irradiance model (Chamberlin et al., 2007,

402   2008) uses a variable mix of observations and indices to provide more realistic solar

403   irradiance spectra. Peterson et al., [2008, 2009, and 2012] have shown that the observed

404   and FLIP/FISM modeled photoelectron energy spectra generally agree to within model

405   and observational uncertainties. Peterson et al. [2012] have shown that on solar rotation

406   time scales about 30% of the observed variability in the photoelectron flux intensity is not

407   captured by the FLIP/FISM or other code/irradiance model pairs investigated. The

408   moderate to strong correlations shown in the fourth column of Table 1 are consistent with

409   the results presented in Peterson et al., [2012].

410   **Discussion:**

411

412   Because the photochemistry of the Martian and Earth ionospheres are not that

413   dissimilar (e.g. Schunk and Nagy, 1980), we can reasonably expect that variations in

414   EUV and XUV irradiance at Mars cause similar variations in photoelectron intensity at

415   Earth. Furthermore the variations in photoelectron intensity at Mars should be correlated

416   to those at Earth when the same side of the solar disk illuminates both planets. We have

417   analyzed data for a time interval when the Earth-Sun-Mars angle is less than 30° and

418   there is moderate activity on the Sun. Table 1 shows that variations in solar irradiance

419   proxies and calculations using the FLIP/FISM model pair are moderately to strongly

420   correlated with variations in observed photoelectron energy spectra in various energy

421   bands. In contrast, Figure 10 and Table 1 demonstrate that there is weak to moderate

422   correlation between variations in photoelectron intensity in selected energy bands at

423   Earth detected on the FAST spacecraft and intensity variations in the photoelectron

424   energy spectra derived from MGS/ER observations at Mars. This level of correlation

425   means that variations of Solar EUV irradiance incident on Mars cannot be reliably

426   monitored by the MGS/ER observations presented above.

427   At Mars identification of photoelectron spectra is made by confirming the presence

428   of one or more features in the electron spectra associated with HeII 30.4 nm emissions,

429   Auger electrons, and the sharp decrease in solar irradiance below ~16 nm. As shown in

430   Figures 5 and 6, the filter we developed to select energy spectra dominated by

431   photoelectrons focuses on pitch angle resolved features associated with the HeII 30.4 nm

432   emissions and the sharp decrease in solar irradiance below ~16 nm. Figures 5 and 6 show

433   that electron energy spectra without the two features are easily identified. Because solar

434   wind electrons can penetrate quite deeply into the ionosphere, Martian electron energy

435   spectra with the two pitch angle resolved features could also include solar wind electrons.

436   We note that the MGS/ER data presented here were acquired at altitudes between 370

437   and 440 km.

438   The analysis and modeling work of Frahm et al., (2007), Liemohn et al., (2003) and

439   others show that identifying photoelectron spectra in electron energy spectra obtained at

440   Mars depends strongly on the altitude of data acquisition, the energy resolution of the

441   detector, and the availability of pitch angle resolved energy spectra. Frahm et al., (2007)

442   used photoelectron energy spectra obtained over a larger altitude range (250-10,000 km)

443   from Mars Express (MEX). They have shown that, except at the lowest altitudes sampled,

444   photoelectron energy spectra are not detected on every orbit. Liemohn et al., (2003) have

445   developed a pitch-angle dependent photoelectron production and transport code. They

446   have identified regions of closed magnetic fields in the MGS/ER data and shown that

447   MGS/ER electron energy and pitch angle observations agreed well with the calculations,

448   considering the uncertainties in the Mars neutral atmosphere and solar irradiance. Their

449   analysis also shows that the most sensitive model/data comparisons are possible when

450   considering nearly magnetic field aligned observations.

451   We conclude that it is not possible to adequately separate photoelectrons and solar

452   wind electrons in the electron spectra obtained by MGS/ER to be able to use them as a

453   monitor of solar variability. The data do not have enough pitch angle resolved energy

454   resolution and are not obtained at low enough altitudes. The MGS/ER data has two pitch

455   angle resolved energy steps in the 20-30 eV region specific to the HeII 30.4 nm emissions

456   and one pitch angle resolved energy step in the 60-70 eV region specific to the sharp drop

457   off in solar irradiance below 16 nm. The filters we have discussed above are not ideal

458   because they have necessarily had to include energy steps outside of the optimal ranges

459   and are obtained well above 250 km where Frahm et al., (2007) have found distinct HeII

460   30.4 nm features in MEX electron spectra on almost every orbit. The Mars electron data

461   passing through our filters thus contains an unknown and variable fraction of solar wind

462   electrons, which is reflected in the weak to moderate correlation with Earth observations

463   shown in Table 1.

464   **Conclusion**
465

466   At Earth photoelectron intensity in selected bands correlates well with calculations

467   based on the FISM model, which is based on observations supplemented by a solar model

468   in the 0-27 nm range. We find that limitations to the identifications of photoelectron

469   energy spectra in MGS/ER data preclude their use as a more reliable monitor of Solar

470   EUV and XUV variability. However, observations obtained at lower altitudes, closer to

471   the peak photoelectron production region, might allow the separation of the solar wind

472   and ionospheric components of electron energy spectra so that they could be used as a

473   more reliable model for variations in solar EUV and XUV irradiance than the time shifted,

474   Earth based, $F_{10.7}$ index currently used. Such higher energy resolution pitch angle

475   resolved observations below 250 km will soon be available on NASA's Mars

476   Atmosphere and Volatile Evolution Mission (MAVEN,

477   http://lasp.colorado.edu/home/maven/) to be launched in late 2013. MAVEN will also

478   carry a solar EUV irradiance monitor providing a direct measure of the solar input in

479   order to validate this relationship. The lack of a magnetometer precludes use of the

480   technique described here for electrons detected on the Mars Express spacecraft (Frahm et

481   al., 2007).

References:

Acuña, M. H., et al., Mars Observer magnetic fields investigation, J. Geophys. Res., 97, 7799, 1992.

Acuña, M. H., et al. (2001), Magnetic field of Mars: Summary of results from the aerobraking and mapping orbits, J. Geophys. Res., 106(E10), 23403–23417, doi:10.1029/2000JE001404.

Brain, D. A., R. J. Lillis, D. L. Mitchell, J. S. Halekas, and R. P. Lin (2007), Electron pitch angle distributions as indicators of magnetic field topology near Mars, J. Geophys. Res., 112, A09201, doi:10.1029/2007JA012435.

Bertaux, Jean-Loup, François Leblanc, Olivier Witasse, Eric Quemerais, Jean Lilensten, S. A. Stern, B. Sandel, and Oleg Korablev (2005), Discovery of an aurora on Mars, *Nature* **435**, 790-794,| doi:10.1038/nature03603

Carlson, C. W., et al. (2001), The electron and ion plasma experiment for FAST, *Space Sci. Rev.*, 98, 33.

Chamberlin, P. C., T. N. Woods, and F. G. Eparvier (2007). Flare Irradiance Spectral Model (FISM): Daily component algorithms and results, *Space Weather*, 5, S07005, doi:10.1029/2007SW000316.

Chamberlin, P. C., T. N. Woods, and F. G. Eparvier (2008). Flare Irradiance Spectral Model (FISM): Flare component algorithms and results, Space Weather, 6, S05001, doi:10.1029/2007SW000372.

Doering, J.P., W.K. Peterson, C.O. Bostrom, and T.A. Potemra (1976), High resolution daytime photoelectron energy spectra from AE-E, Geophys. Res. Lett. 3, 129.

Dubinin, E., M. Fränz, J. Woch, E. Roussos, S. Barabash, R. Lundin, J. D. Winningham, R. A. Frahm and M. Acuña (2006), Plasma Morphology at Mars. Aspera-3 Observations, Space Sci. Rev. 126, 209, doi: 10.1007/s11214-006-9039-4.

Dubinin, E., et al. (2008), Plasma environment of Mars as observed by simultaneous MEX-ASPERA-3 and MEX-MARSIS observations, *J. Geophys. Res.*, 113, A10217, doi:10.1029/2008JA013355.

Fox, J. L. and K. E. Yeager (2006), Morphology of the near-terminator Martian ionosphere: A comparison of models and data, *J. Geophys. Res.*, *111*, A10309, doi:10.1029/2006JA011697.

Frahm, R.A., et al., (2006), Carbon dioxide photoelectron energy peaks at Mars, Icarus, 182, 371, doi: 10.1016/j.icarus.2006.01.014.

530   Frahm, R.A., J. R. Sharber, J. D. Winningham, P. Wurz, M. W. Liemohn, E. Kallio,
531   M. Yamauchi, R. Lundin, S. Barabash, A. J. Coates, D. R. Linder, J. U. Kozyra,
532   M. Holmström, S. J. Jeffers, H. Andersson and S. Mckenna-Lawler (2007),
533   Locations of Atmospheric Photoelectron Energy Peaks Within the Mars
534   Environment, Space Sci. Rev. 126, 389, doi: 10.1007/s11214-006-9119-5.
535
536   Gronoff, G., C. Simon Wedlund, C. J. Mertens, and R. J. Lillis (2012), Computing
537   uncertainties in ionosphere-airglow models: I. Electron flux and species production
538   uncertainties for Mars, J. Geophys. Res., 117, A04306, doi:10.1029/2011JA016930.
539
540   Jain, S. K., and A. Bhardwaj (2011), Impact of solar EUV flux on CO Cameron band and
541   CO2+ UV doublet emissions in the dayglow of mars, Plan. Sp. Sci., doi:
542   10.1016/j.pss.2011.08.010.
543
544   Lee, J.S., J.P. Doering, T.A. Potemra, and L.H. Brace (1980a), Measurements of the
545   ambient photoelectron spectrum from Atmosphere Explorer: I. AE-E measurements
546   below 300 km during solar minimum conditions, Planet. Space Sci. 28, 947.
547
548   Lee, J.S., J.P. Doering, T.A. Potemra, and L.H. Brace (1980b), Measurements of the
549   ambient photoelectron spectrum from Atmosphere Explorer: II. AE-E measurements
550   from 300 to 1000 km during solar minimum conditions, Planet. Space Sci. 28, 973.
551
552   Liemohn, M. W., D. L. Mitchell, A. F. Nagy, J. L. Fox, T. W. Reimer, and Y. Ma (2003),
553   Comparisons of electron fluxes measured in the crustal fields at Mars by the MGS
554   magnetometer/electron reflectometer instrument with a B field–dependent transport
555   code, J. Geophys. Res., 108(E12), 5134, doi:10.1029/2003JE002158.
556
557   Mitchell, D. L., R. P. Lin, H. Rème, D. H. Crider, P. A. Cloutier, J. E. P. Connerney, M. H.
558   Acuña, and N. F. Ness (2000), Oxygen auger electrons observed in Mars'
559   ionosphere, *Geophys. Res. Lett.*, 27(13), 1871–1874,
560   doi:10.1029/1999GL010754.
561
562   Mitchell, D. L., R. P. Lin, C. Mazelle, H. Rème, P. A. Cloutier, J. E. P. Connerney, M. H.
563   Acuña, and N. F. Ness (2001), Probing Mars' crustal magnetic field and
564   ionosphere with the MGS Electron Reflectometer, *J. Geophys. Res.*, 106(E10),
565   23,419–23,427, doi:10.1029/2000JE001435.
566
567   Peterson, W.K., P.C. Chamberlin, T.N. Woods, and P.G. Richards (2008). Temporal and
568   spectral variations of the photoelectron flux and solar irradiance during an X class
569   solar flare, *Geophys. Res. Lett.*, 35, L12102, doi: 10.1029/2008GL033746.

570   Peterson, W.K., E.N. Stavros, P.G. Richards, P.C. Chamberlin, T.N. Woods, S.M. Bailey,
571   and S.C. Solomon (2009), Photoelectrons as a tool to evaluate spectral variations in
572   solar EUV irradiance over solar cycle time scales, *J. Geophys. Res.*, 114, A10304,
573   doi:10.1029/2009JA014362.

574   Peterson, W. K., T. N. Woods, J. M. Fontenla, P. G. Richards, P. C. Chamberlin, S. C.

575   Solomon, W. K. Tobiska, and H. P. Warren (2012), Solar EUV and XUV energy
576   input to thermosphere on solar rotation time scales derived from photoelectron
577   observations, *J. Geophys. Res.*, *117*, A05320, doi:10.1029/2011JA017382.
578

579 Qian, L., A. G. Burns, P. C. Chamberlin, and S. C. Solomon (2010), Flare location on the
580   solar disk: Modeling the thermosphere and ionosphere response, J. Geophys. Res.,
581   115, A09311, doi:10.1029/2009JA015225.

582 Richards, P. G. (2001), Seasonal and solar cycle variations of the ionospheric peak
583   electron density: Comparison of measurement and models, J. Geophys. Res., 106,
584   12,803.

585 Richards, P. G. (2002), Ion and neutral density variations during ionospheric storms
586   in September 1974: Comparison of measurement and models, J. Geophys. Res.,
587   107(A11), 1361, doi:10.1029/2002JA009278.

588 Richards, P. G. (2004), On the increases in nitric oxide density at midlatitudes during
589   ionospheric storms, J. Geophys. Res., 109, A06304, doi:10.1029/2003JA010110.

590 Richards, P.G., T.N. Woods, and W.K. Peterson (2006). HEUVAC: A new high
591   resolution solar EUV proxy model, *Adv. Space Res.,* 37, 315–322,
592   doi:10.1016/j.asr.2005.06.031.

593 Richards, P. G., and W. K. Peterson (2008), Measured and modeled backscatter of
594   ionospheric photoelectron fluxes, J. Geophys. Res., 113, A08321,
595   doi:10.1029/2008JA013092

596 Schunk, R.W., and A.F. Nagy (1980), Ionospheres of the terrestrial planets, *Rev.*
597   *Geophys. and Space Phys.*, 18, 813-852.

598 Solomon, S. C., and L. Qian (2005), Solar extreme-ultraviolet irradiance for general
599   circulation models, J. Geophys. Res., 110, A10306, doi:10.1029/2005JA011160.

600 Ulrich, R.K., and J.E. Boyden (2006), Carrington Coordinates and Solar Maps, Solar
601   Physics, 235, 17-29, doi:10.1007/s11207-006-0041-5

602 Woods, T. N., F. G. Eparvier, S. M. Bailey, P. C. Chamberlin, J. Lean, G. J. Rottman, S. C.
603   Solomon, W. K. Tobiska, and D. L. Woodraska (2005), Solar EUV Experiment
604   (SEE): Mission overview and first results, J. Geophys. Res., 110, A01312,
605   doi:[10.1029/2004JA010765](10.1029/2004JA010765).

606 Woods, T. N., F. G. Eparvier, R. Hock, A. R. Jones, D. Woodraska, D. Judge, L.
607   Didkovsky, J. Lean, J. Mariska, H. Warren, D. McMullin, P. Chamberlin, G.
608   Berthiaume, S. Bailey, T. Fuller-Rowell, J. Sojka, W. K. Tobiska, and R. Viereck
609   (2010), "Extreme Ultraviolet Variability Experiment (EVE) on the Solar
610   Dynamics Observatory (SDO): Overview of Science Objectives, Instrument
611   Design, Data Products, and Model Developments", Solar Physics, p. 3, doi:
612   10.1007/s11207-009-9487-6.

613 **Table:**

614

615

Band Center (nm)	Band Center (eV)	Earth- Mars	Earth – FLIP/FISM Calculation	Earth – $F_{10.7}$	Earth - GOES Max	Earth - MgII index
3	385	0.43	0.65	0.64	0.32	-0.48
7	156	0.57	0.40	0.69	0.24	-0.65
13	77	0.20	0.93	0.17	-0.03	-0.45
22.5	38	0.34	0.85	-0.01	-0.15	-0.42
38.5	16	0.48	0.76	0.26	-0.06	-0.60

616 Table 1: Correlation coefficients between Photoelectron observations, and calculations
617 and EUV/XUV proxies for the interval September 1 to October 15, 2005 for five selected
618 energy bands.

619   **Figures:**

620
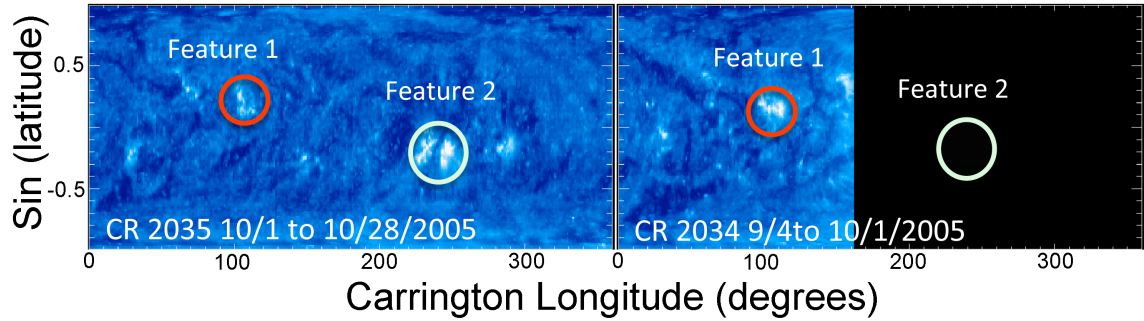
621

622   Figure 1. Data from the SOHO 17.1 nm imager for two Carrington rotations. Data
623   are presented as a function of the sine of solar latitude and Carrington longitude. Note
624   that in this format time goes from right to left. SOHO data were not available before 9/15
625   as indicated by the lack of data in Carrington rotation 2034 from longitudes 360-160.

626

627
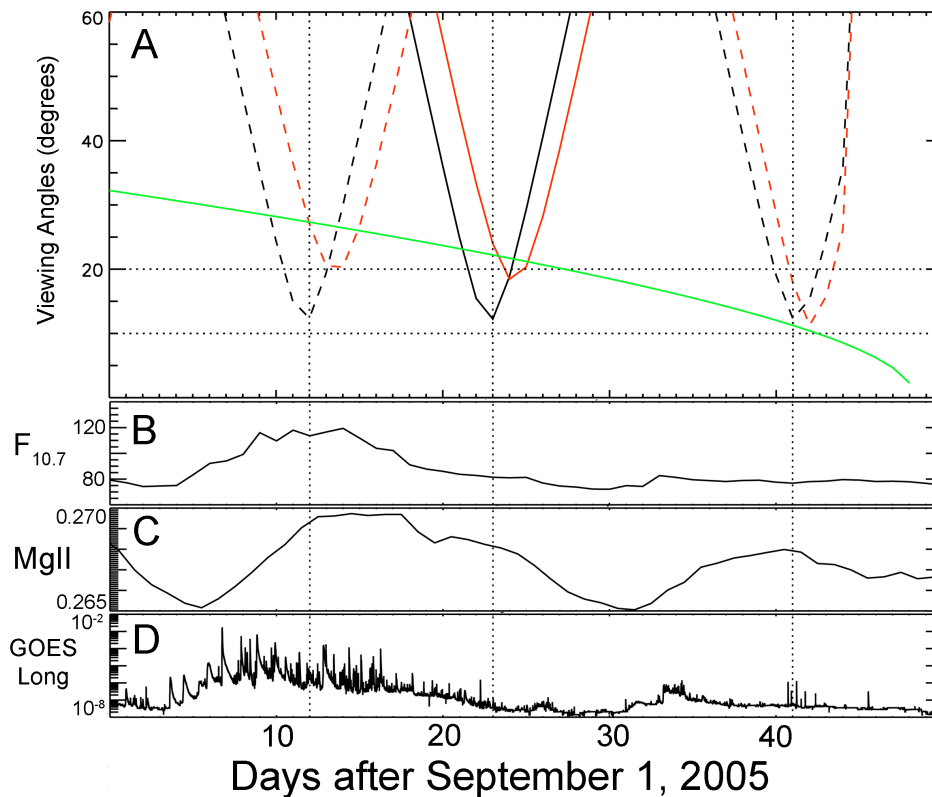
Figure 2. Further details of solar activity as seen on Earth and Mars. A) Viewing angles: The green line shows the Earth-Sun-Mars angle in degrees as a function of time. The other lines indicate the angles of the two solar features identified in Figure 1 as seen from Earth and Mars. Red lines indicate Mars; black lines indicate Earth. Feature 1 is shown in solid lines; feature 2 is shown with dotted lines. The dotted vertical lines appear for September 13 and 24 and October 12, the days the features identified in Figure 1 are closest to the center of the Sun's disk observed from Earth. Note that the time interval shown in Figure 2 is shorter than that shown in Figure 1. B) Solar $F_{10.7}$ index values in solar flux units (10^{-22} W m^{-2} Hz^{-1}). C) The non-dimensional solar magnesium II index (core-to-wing ratio at 280 nm) values. D) GOES long values: Intensity of the 0.7 nm X-ray intensity observed by one of NOAA's GOES satellites. The logarithmic scale covers the range from 10^{-8} to 10^{-2} W/m^2

641
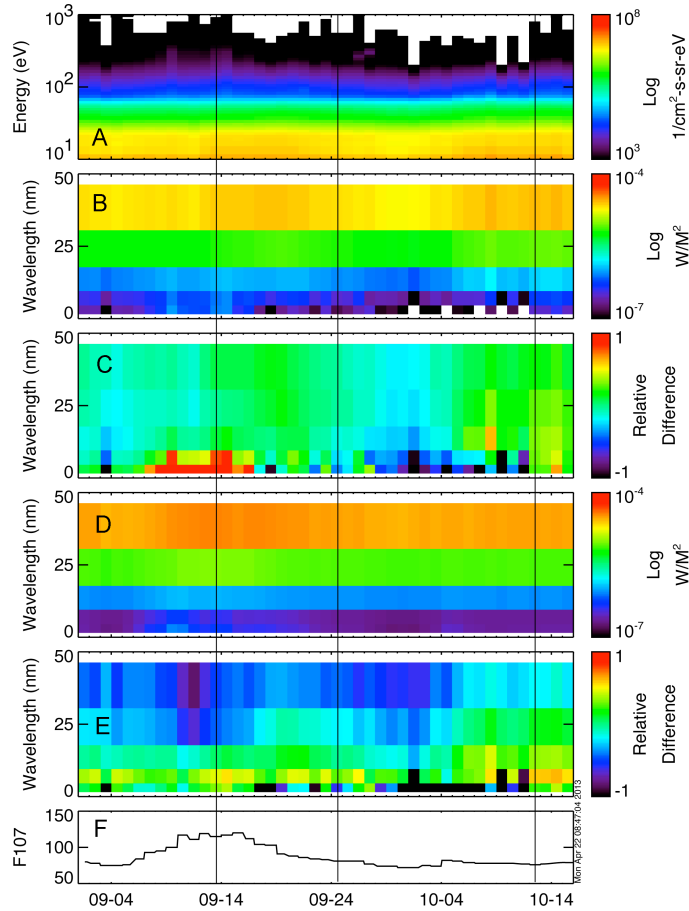
Figure 3: Observed and modeled terrestrial photoelectron energy spectra from September 1 to October 16, 2005. Vertical black lines are drawn for September 13 and 24 as well as October 12. A) Daily average of the observed photoelectron flux encoded using the color bar on the right as a function of energy. B) Daily average of the observed photoelectron power density 5 equivalent wavelength bands. The power density in units of W/m^2 is encoded by the color bar on the right. C) Relative difference between the observations shown in panel B and the average as a function of equivalent wavelength observed over the entire interval encoded using the color bar on the right. D) Calculated daily average photoelectron power density in the same 5 equivalent wavelength bands used in panel C. The power density is encoded using the color bar on the right. E) Relative difference encoded using the color bar on the right using between the observations seen in Panel B and the calculation seen in panel D. F) Daily solar $F_{10.7}$ index.

655

656
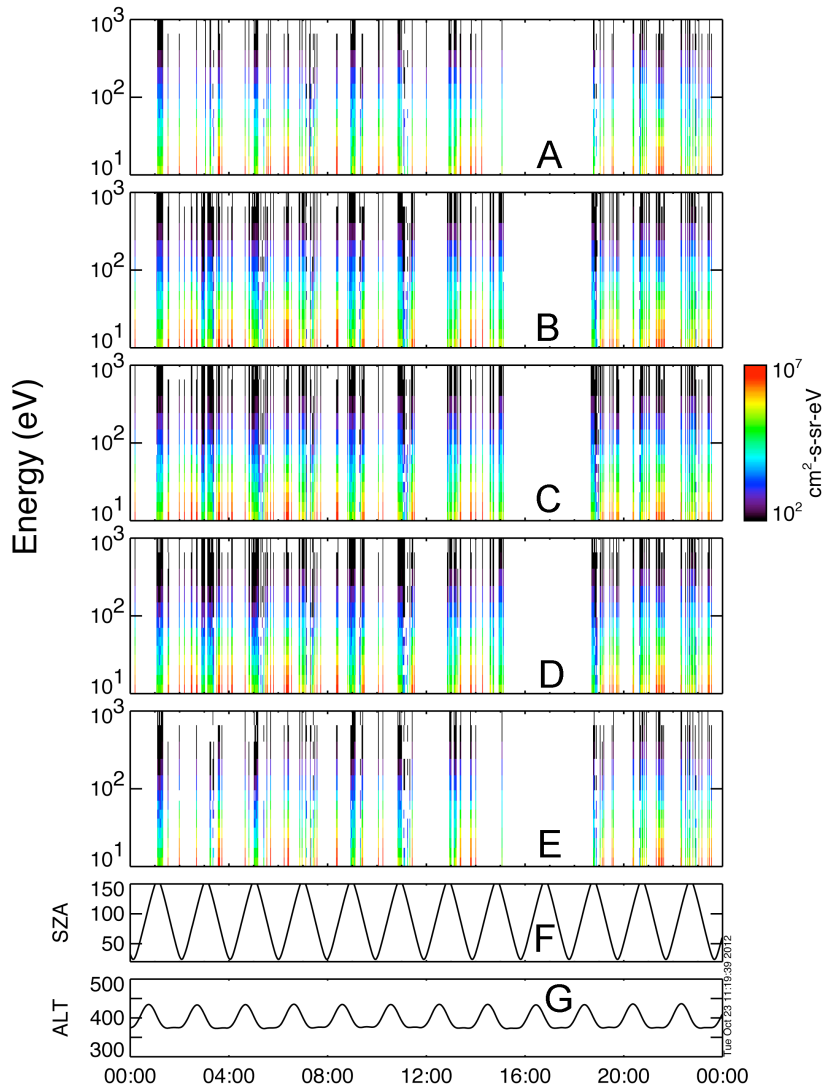
Figure 4: Pitch angle resolved energy spectra obtained on September 20, 2005 from the MGR/ER instrument. Panels A-E display electron energy spectra as a function of time with the intensity encoded in units of $(cm^2\text{-s-sr-eV})^{-1}$ using the color bar on the right. Panels A-E display pitch angle ranges $0\text{-}30^o$, $30\text{-}60^o$, $60\text{-}120^o$, $120\text{ -}150^o$, and $150\text{ -}180^o$ respectively over the energy range from 10 eV to 1 keV. F) The solar zenith angle in degrees at the location where the electron spectra were obtained. G) The altitude in km at the location the location where the electron spectra were obtained.

664

665
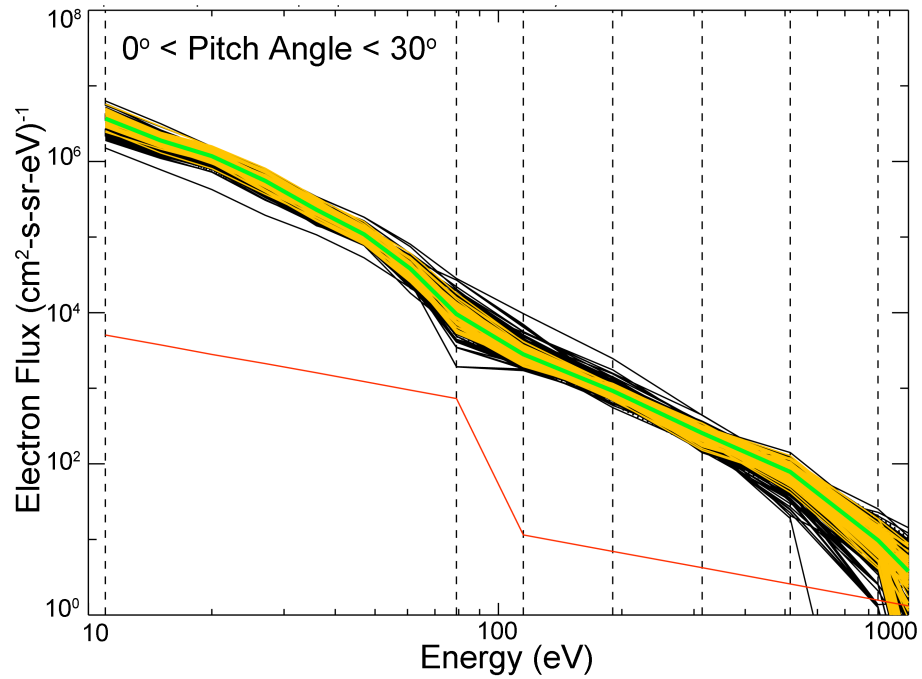
Figure 5: Partially filtered MGR/ER electron spectra for September 20, 2005. The 106 electron spectra passing the energy step filter are shown in orange. The average of these 106 spectra is shown as a solid green line. The solid red line shows the instrumental background (dominated by penetrating particles). See text.

670

671
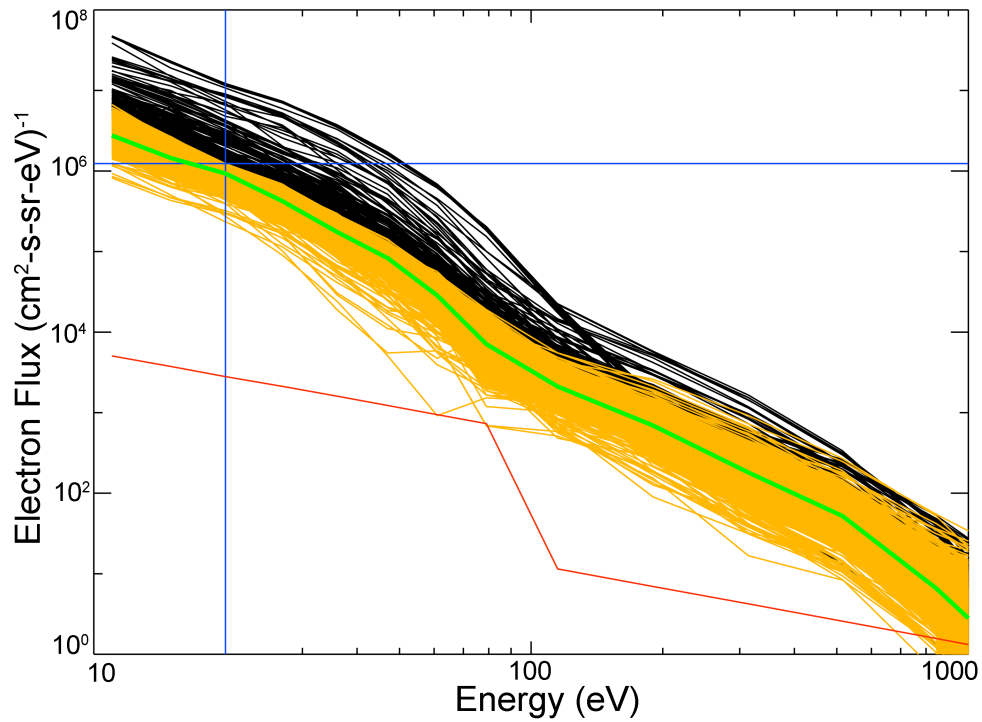
Figure 6. The 7353 electron spectra in the 0º to 30º range passing the daily
shape filter between September 14 and December 15, 2005. A third filter, described
in the text, selects 6603 for further processing. The selected spectra are shown in
orange. The average of the selected spectra is shown as a green line. The solid red
line is the detection threshold.

677

678
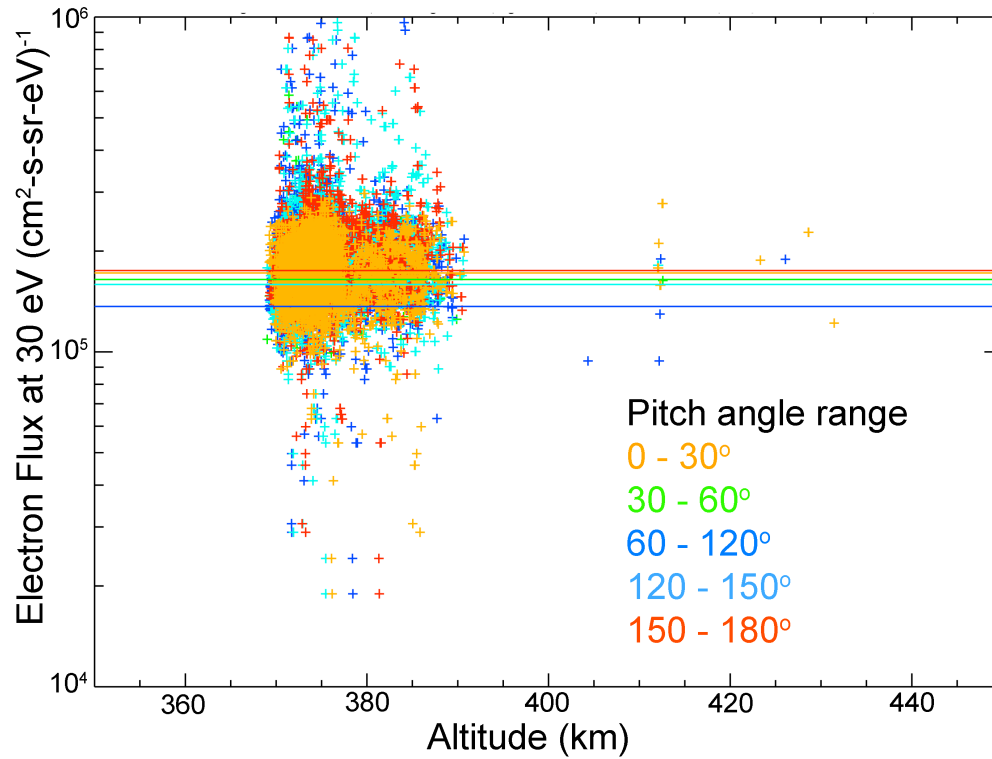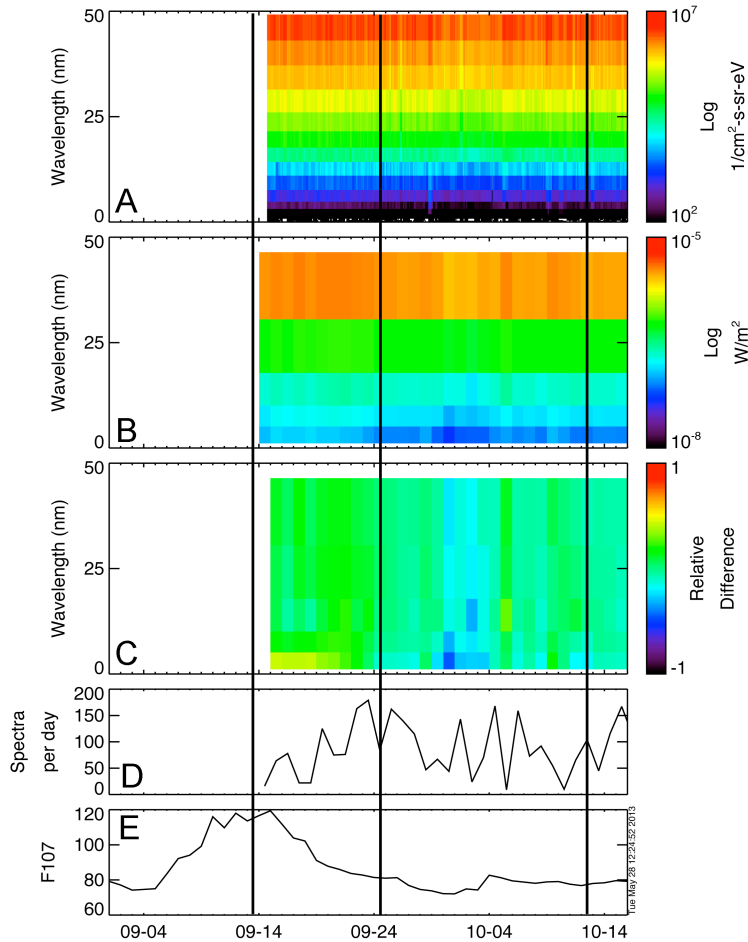
Figure 7. Scatter plots of the flux intensity at 30 eV as a function of altitude for the color-coded pitch angle ranges indicated. The color-coded solid horizontal lines show the average flux for the indicated pitch angle ranges.

682

683

Figure 8. Observed Martian daily photoelectron energy spectra from September 15 to October 16, 2005 for the time range shown in Figure 3. No daily average MGS/ER in the 0-30° pitch angle range are available from September 1 to14. Vertical black lines are drawn for September 13 and 24 as well as October 12. A) All observed photoelectron flux observations encoded using the color bar on the right as a function of energy. B) Daily average of the observed photoelectron power density 5 equivalent wavelength bands. The power density in units of W/m^2 is encoded by the color bar on the right. C) Relative difference between the observations shown in panel B and the average as a function of equivalent wavelength observed over the entire interval encoded using the color bar on the right. D) Number of photoelectron spectra included in the daily average. E) Daily solar $F_{10.7}$ index.

695

696
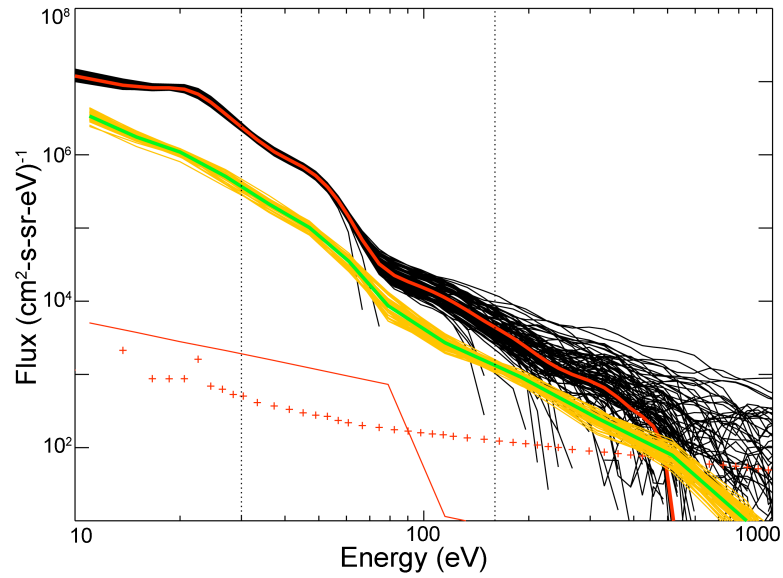
Figure 9. Photoelectron spectra acquired on the FAST satellite at Earth (black) and on the MGS satellite at Mars in the pitch angle range 0-30° on September 20, 2005. The average Earth spectrum is shown in red and the average Mars spectrum is shown in green. . The red + symbols show the 1 standard deviation uncertainty in the average Earth flux value based on the number of counts detected. The solid red line at the bottom is the instrument background of the Mars electron detector. The vertical dotted lines are at 30 and 110 eV as they are in Figure 6.

704

705
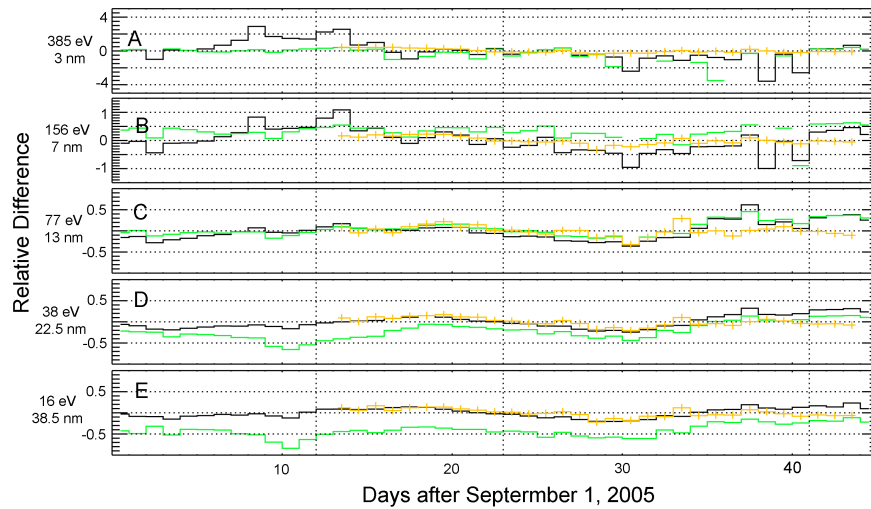
Figure 10: Relative difference between photoelectrons in 5 energy bands observed
at Earth (black) and Mars (orange) and calculated for Earth (green) for 45 days
starting on September 1, 2005. The center energy and equivalent wavelength are
shown on the left for each band. The relative difference is the observed/calculated
value – average divided by the average. Note that the scale of relative differences is
+/- 4 in panel A, +/- 1.5 in panel B and +/- 0.5 in Panels C, D, and E. The dotted
vertical lines appear for September 13 and 24 and October 12, the days the features
identified in Figure 1 are closest to the center of the Sun's disk observed from Earth.